



Highly sensitive fiber Bragg grating-based pressure sensor using side-hole packaging

SUNEETHA SEBASTIAN,^{1,†} S. SRIDHAR,^{1,†} P. SHIVA PRASAD,² AND S. ASOKAN^{1,*}

¹Department of Instrumentation and Applied Physics, Indian Institute of Science, Bangalore, India

²Research Center Imarat, DRDO, Hyderabad, India

*Corresponding author: sasokan@iisc.ac.in

Received 6 September 2018; revised 7 November 2018; accepted 7 November 2018; posted 8 November 2018 (Doc. ID 343102); published 20 December 2018

In this work, an analysis of pressure response of a fiber Bragg grating (FBG) sensor in a side-hole package is presented using the finite element method. Various parameters of the side-hole packaging such as hole radius, the distance of separation between them, the radius and length of the package, and the choice of the package material are considered and optimized in order to promote maximum pressure sensitivity of the FBG sensor. This investigation on optimization of the side-hole package parameters gives rise to pressure sensitivity of nearly 10^5 times as compared with the bare FBG sensor, with the numerical values of 3 pm/MPa for a bare FBG sensor to $\sim 280,000$ pm/MPa for an optimized side-hole package FBG sensor. Such high-pressure sensitivity of an FBG sensor is being reported for the very first time in this work, to the best of our knowledge, and can be considered as the initial step toward the realization of a highly sensitive hydrophone based on FBG for sensing underwater acoustic signals. © 2018 Optical Society of America

<https://doi.org/10.1364/AO.58.000115>

1. INTRODUCTION

Optical fiber-based hydrophones, an acoustic signal detector, have been widely studied for their extensive uses in various fields such as military sonars [1], geophysical [2], and marine monitoring [3]. To compare with conventional piezo-based sensors, fiber-based hydrophones inherit the advantages of more flexibility, light weight, low cost, and complete immunity to electromagnetic interference. Further, optical fiber-based hydrophones require no electrical components in the sensing area, which provides a completely passive network of sensors. However, in ordinary optical fiber sensors, the measured phase/amplitude/wavelength shift of transmitting optical signal gives the information about various measurands. On the other hand, an FBG sensor uses the reflection of narrow wavelength bandwidth in its process of measurement of various measurand [4], which is a more direct and unwavering measurement than that of phase shift. FBG sensors also possess several added advantages such as reliability and stability in severe environments, smaller size, and multiplexing capability over conventional sensors. Whenever acoustic pressure is imposed on an FBG sensor, the resultant strain is induced in the core of the fiber, which ultimately alters the grating pitch and yields a shift in Bragg wavelength. Because the optical fiber material possesses high Young's modulus (nearly 72 GPa), the deformations due to the applied pressure on the grating are feeble. Previous studies measure 3 pm of shifts in the Bragg wavelength when a pressure of 1 MPa is applied on a bare FBG sensor [5]. This prevents the FBG sensors from

large deformation under acoustic pressure [6]. This eventually results in the low sensitivity of the FBG-based sensors in their use in underwater applications.

To extend the application of FBG sensors for deep sea applications such as underwater acoustic sensing, it demands the enhancement of pressure sensitivity of FBG by several orders of magnitude (such that FBG can detect acoustic signal in mPa range). The resolution of the FBG interrogator (wavelength demodulator) is the central unit, which defines the pressure sensitivity of the FBG sensor. But the typical resolution of the commercially available FBG sensor systems is $\cong 1$ pm/ μe , which is possible to detect the pressure of, is in the range of MPa. Hence, the appropriate development of interrogator sensitivity and/or amplification of the FBG sensor's pressure sensitivity have to be achieved to suit underwater acoustic pressure sensing. In consideration of improvement of the FBG sensor's pressure sensitivity, a number of efforts have been taken such as by coating FBG sensors with polymeric material [6], using phase-shifted FBGs [7,8], using a distributed feedback (DFB) fiber laser [9,10], using photonic crystal fiber [11], etc. Apart from those techniques, Xie *et al.* [12] have proposed side-hole fibers as a feasible hydrostatic or acoustic pressure sensor. In the side-hole fibers, due to the introduction of holes in the fiber, which breaks the mechanical symmetry of the fiber, the symmetrical stress/pressure induced by hydrostatic pressure on the surface of the fiber is transferred as an amplified asymmetrical stress distribution in the fiber core [13]. Further, the applied pressure is measured

from the birefringence in the core, which is governed by the photo-elastic property of the fiber, induced by the applied asymmetrical stress distribution [14–16]. Considering this concept, researchers developed the novel side-hole package [17–19] for FBG-based hydrostatic pressure sensors. However, in the previous studies, a systematic study on a side-hole package for maximum pressure amplification in FBG sensor has not been reported.

The present work deals with a systematic approach on a side-hole packaged FBG sensor to achieve maximum pressure amplification in the fiber core. Different parameters, involving the determination of the pressure sensitivity enhancement of an FBG sensor such as package dimensions and its materials, have been optimized theoretically using COMSOL Multiphysics software. In this cautious, systematic study, by the precise investigation of all the parameters of the side-hole package, the highest ever reported sensitivity pressure enhancement of the order of 10^5 times, to compare with the typical bare FBG sensor, has been achieved. Apart from enormous pressure amplification on FBG sensors, this package also offers an additional advantage by providing more mechanical stability to the fiber. Because the package emanates with additional features such as mechanical stability, the possibility of incorporating different types of sensors, such as etched FBGs, etched FBGs coated with nanomaterials, etc., which has improved pressure sensitivity over that of the typical bare FBG sensor, can be considered in the future.

2. SIMULATION METHOD AND THEORY

Figure 1 depicts the side-hole package of silica fiber for pressure/stress amplification, where R is the outer radius of the side-hole package, L is the length of the package, R_h is the radius of the hole, and d is the distance of separation between the two side holes. A single-mode fiber with a core and a cladding diameter of 8 and 125 μm , respectively, has been chosen for the present studies (mechanical and optical properties of the fiber are listed in Table 1). The fiber core diameter has been preferred to confine to the propagation of only fundamental mode (LP_{01}) through it.

In the preliminary simulations, the parameters of the side-hole package such as R , R_h , and L have been chosen as 10, 3, and 20 mm, respectively, with polyimide as the packaging material (material properties are listed in Table 2). Bragg

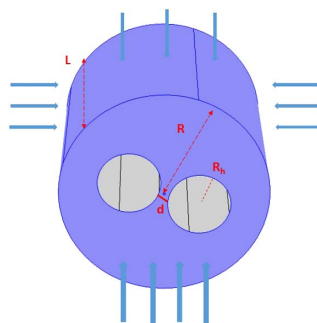


Fig. 1. Schematic structure of the side-hole package of single-mode silica fiber. Holes are symmetrical, and fiber is at the center of the package. Pressure is applied on the surface side-hole package both radially and axially. Arrows show the direction of pressure.

Table 1. Mechanical and Optical Properties of Silica Fiber

Properties of Silica Fiber	Values
Young's modulus (E_{SiO_2})	73.1 GPa
Poisson's ratio (ν_{SiO_2})	0.17
Density (ρ_{SiO_2})	2203 Kg/m ³
Refractive index of the core (n_0)	1.456
Refractive index of cladding (n_1)	1.445

Table 2. Mechanical Properties of Packaging Materials

Properties	Polyimide	RTV3145
Young's modulus	2.5 GPa	1.1 MPa
Poisson ratio	0.47	0.42
Density	1420 Kg/m ³	1120 Kg/m ³

gratings are simulated, in the middle of the fiber core, with a length of 1 mm and a grating period [pitch (Λ)] of 532 nm. Figure 2 shows the modulated refractive index due to grating along the fiber core, where the index profile takes the form as given by [20]

$$n(z) = n_0 + \delta n [\cos(2\pi z/\Lambda) + 1]. \quad (1)$$

Here, n_0 , δn , and z represent the unperturbed refractive index of the core, the amplitude of the photoinduced index change, and longitudinal direction along the fiber, respectively, and Λ is the pitch of the grating. The refractive index is modulated to be between 1.456 and 1.4574 in this current study. This index modulation is responsible for the coupling of the forward-propagating LP_{01} mode to backward propagating LP_{01} mode,

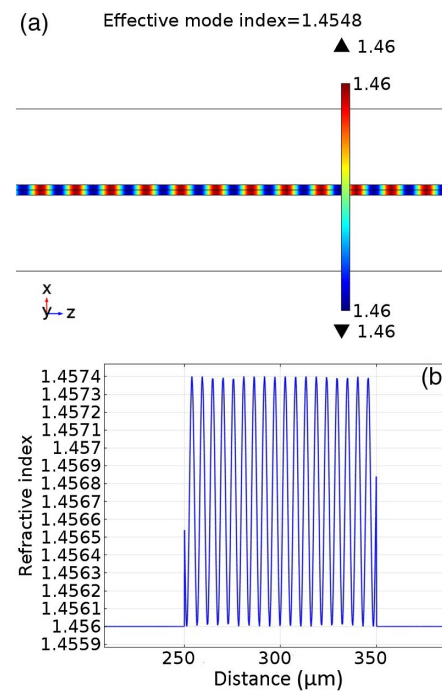


Fig. 2. (a) Simulated image of FBG in the core of the fiber with a pitch of 532 nm. (b) Line graph of modulated refractive index versus length of the grating.

thereby causing a reflection. It is well known that the Bragg (reflected) wavelength (λ_B) depends on two main parameters (n_{eff} and Λ), in the following manner:

$$\lambda_B = 2n_{\text{eff}}\Lambda, \quad (2)$$

where n_{eff} is the effective refractive index of the LP_{01} mode propagating in the fiber.

Under external perturbation, such as strain and/or temperature, both the above-mentioned parameters experience a variation. Hence, there is an alteration in the Bragg wavelength. This difference corresponds to the amount of external perturbation. External strain field changes the response of FBG directly through the change in the grating pitch dimension and through the strain-optic effect [21] given as

$$\Delta\lambda_B = \lambda_B(1 - \rho_e)\varepsilon, \quad (3)$$

where ρ_e is the photo-elastic coefficient, and ε is the longitudinal strain on the gratings.

In this simulation work, application of external pressure and the subsequent alteration in the Bragg wavelength has been carried out in two major parts. In the first part, the stress and strain distribution along the fiber cross-section and its geometrical deformation are simulated using the structural mechanics module of COMSOL Multiphysics software. The impact of pressure along the cross-section of the fiber has been analyzed using the surface plot of the Von Mises stress distribution. The Von Mises stress parameter (σ_{VM}) is calculated from the normal stresses (σ_{XX} , σ_{YY} , σ_{ZZ}) and shear stresses (τ_{XY} , τ_{YZ} , τ_{ZX}) along the x , y , and z axes of the system, as given in the equation below:

$$\sigma_{VM} = \sqrt{\frac{1}{2}((\sigma_{XX} - \sigma_{YY})^2 + (\sigma_{YY} - \sigma_{ZZ})^2 + (\sigma_{ZZ} - \sigma_{XX})^2)} + 3(\tau_{XY}^2 + \tau_{YZ}^2 + \tau_{ZX}^2). \quad (4)$$

The output obtained from this module is fed to the following equations to acquire the refractive-index profile in the fiber structure using the photo-elastic relations [22]:

$$n_x = n_0 - B_1 S_x - B_2(S_y + S_z), \quad (5a)$$

$$n_y = n_0 - B_1 S_y - B_2(S_x + S_z), \quad (5b)$$

$$n_z = n_0 - B_1 S_z - B_2(S_x + S_y). \quad (5c)$$

Here, B_1 and B_2 are the stress-optic coefficients of silica, given by $6.5e - 13 \text{ m}^2/\text{N}$ and $4.2e - 12 \text{ m}^2/\text{N}$ respectively, and S_x , S_y , S_z are the principal stress components along the x , y , and z directions. In the second part, the refractive-index profile, expressed by the Eqs. (5a)–(5c), is given as the input to simulate the effective refractive index (n_{eff}^\dagger) of the LP_{01} mode under pressure using the electromagnetic module of COMSOL. The final equation governing pressure-induced wavelength change is given by [23]

$$\Delta\lambda_B = \lambda_B \left(\frac{\Delta n_{\text{eff}}}{n_{\text{eff}}} + \varepsilon_{z,\text{core}} \right), \quad (6)$$

where $\Delta n_{\text{eff}} = n_{\text{eff}}^\dagger - n_{\text{eff}}$ is the pressure-induced effective index change, and $\varepsilon_{z,\text{core}}$ is the principal strain along the z direction in the fiber core. All the simulations are carried out on a 3D model. A pressure of 100 hPa is applied to the structure with proper secure constraints. The pressure is applied simultaneously both

radially and axially, keeping the inner portion of the side-holes free from pressure, as shown in Fig. 1. After preliminary simulations, by fixing the initial parameters as mentioned in the previous section, these present simulation segments are carried out by varying the parameters of the side-hole package, to optimize the dimensions and material of the package for maximum pressure amplification in the fiber. The pressure amplification factor is defined as the pressure applied on the outer surface of the side-hole package to the pressure generated at the core of the fiber. The following are the parameters of side-hole package, which experienced variations to exhibit maximum pressure amplification:

- (a) Distance between the two holes (d)
- (b) Radius of the holes (R_h)
- (c) Length of the package (L)
- (d) Outer radius of the package (R)
- (e) Package material

3. RESULTS AND DISCUSSION

Stress analysis of fiber in the side-hole package is simulated with initial conditions, as mentioned above (R , 10 mm; R_h , 3 mm; and L , 20 mm).

A. Distance between the Holes

Side-holes of 3 mm radius are symmetrically placed with fiber at the center of the package. It can be seen from Fig. 3 that positioning the holes in the package plays a crucial role in the stress amplification in the fiber core. As the holes are kept away from the fiber, at 7 mm from each other, closer to the outer region of the package, the package yields an amplification of about 1.6 times. Further, when the holes are moved symmetrically toward the center, near fiber, the amplification increases

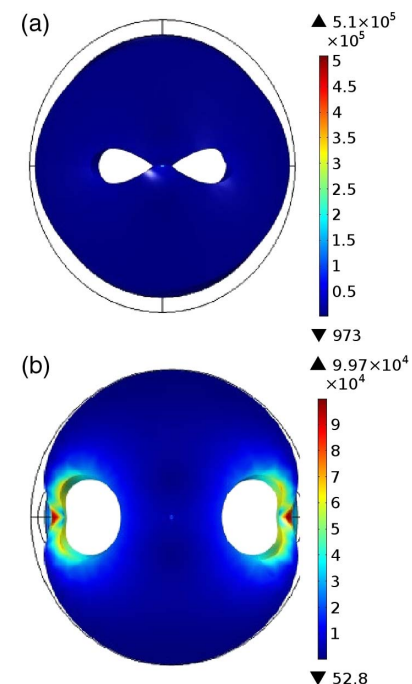


Fig. 3. Surface plot of Von Mises stress (N/m^2) distribution of the package and in the fiber when the distance of separation between the holes is (a) 500 μm and (b) 7000 μm .

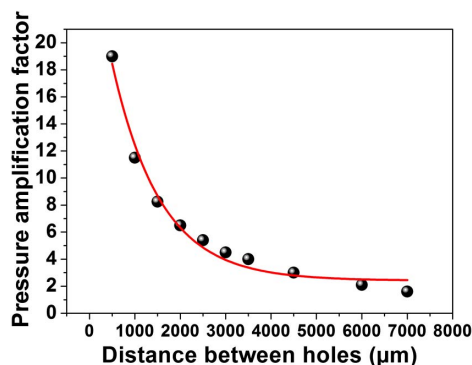


Fig. 4. Plot of pressure amplification factor along the fiber with varying distance of separation between the side-holes for an applied pressure of 100 hPa. Red line corresponds to exponential decay fit.

exponentially, and, at 500 μm distance from each other (simulation limit), an amplification of stress around 20 (i.e., 2000 hPa) times are noticed. This enhancement in strain amplification is attributed to the minimum pressure on the side-holes and maximum along the cross-section of the fiber, as the holes are closer to the fiber [Fig. 3(a)]. Also, the deformation of the spherical geometry of the side-holes arises more as the holes are moved closer to the fiber. Stress along the fiber with respect to the distance of separation between the holes is shown in Fig. 4. The plot is fitted with an exponential decay curve, which indicates that, when the distance of separation between the holes is increased, pressure/stress amplification diminishes exponentially. From this, it is inferred that, for the maximum stress amplification, the side-holes should be placed as close as possible toward the fiber.

B. Radius of the Side-Holes

From the above results, now the distance of separation between the holes is kept constant at 1000 μm (an experimental limitation), and the hole radius is varied from 1 to 4.5 mm; here, 4.5 mm is the maximum possible size of a package of outer radius of 10 mm. Figure 5 shows the Von Mises stress distribution in the side-hole packaged fiber with different hole radii. The hole is completely collapsed when the radius is 1 mm; still, it could show three times stress amplification. With the increase in hole radius, there is a linear increase in the amplification factor, and, as the hole radius approaches 4.5 mm, the maximum stress amplification of 22 times is observed. Also, it can be seen that, in all cases, the spherical geometry deforms under external pressure. Figure 6(a) shows the increasing trend of pressure amplification with respect to increasing hole radius.

This implies that the side-hole package will provide pressure amplification in the fiber irrespective of the size of the hole. For a 1 mm hole radius, the stress amplification of three times is noticed at separation of 1000 μm. Figure 6(b) depicts the stress distribution inside the fiber. As can be seen, the maximum stress is felt along the fiber core when external pressure is applied on the package.

C. Outer Radius of the Package

The maximum stress amplification is noticed when the side-hole size is kept maximum, and a least distance of separation

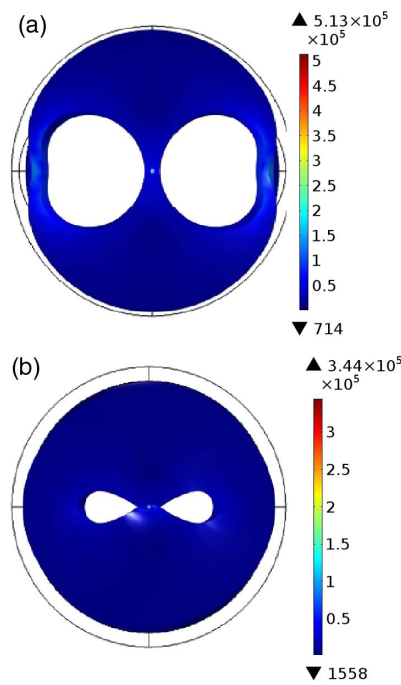


Fig. 5. Surface plot of Von Mises stress (N/m^2) distribution of the package and in the fiber with varying hole diameter of (a) 4.5 mm and (b) 3 mm.

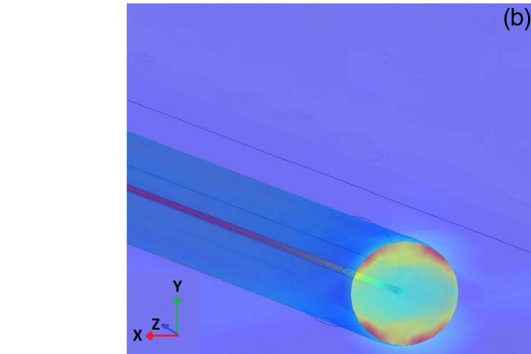
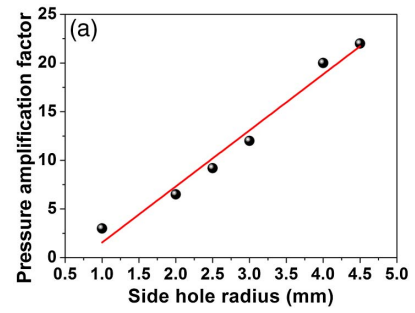


Fig. 6. (a) Plot of pressure amplification factor along the fiber with varying hole radius. Red line indicates the linear fit. (b) Stress distribution inside the fiber. Red color indicates areas of maximum stress, whereas blue indicates minimum.

between them (1000 μm) is maintained for a given outer radius of the package. In this section, the effect of the outer radius of the side-hole package, which can allow the increase of side-hole

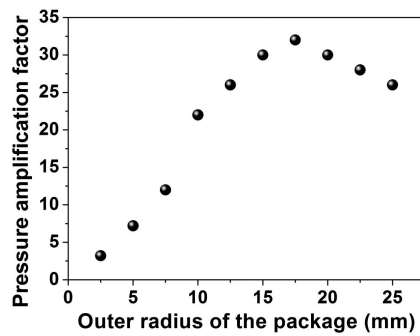


Fig. 7. Plot of pressure amplification factor in the fiber core with varying package radius.

size, has been analyzed. The outer radius of the package is varied from 2.5 to 25 mm, where, in all cases, it is taken care that the side-hole size is kept maximum, and the least distance between them is maintained for the maximum amplification. Unlike from the previous trends, as the outer radius is increased, initially the amplification factor also gradually increases and reaches a maximum value at particular radius; but, further increase in the outer radius results in a decrease in the amplification factor. The maximum amplification of stress, 32 times, is noticed when the package radius is 17.5 mm (with R_b of 8.25 mm). Figure 7 shows the plot of stress amplification factor in the fiber core with varying package radius.

D. Length of the Package

Length of the package is varied from 10 to 30 mm for an outer radius of 17.5 mm, and all other parameters are kept constant (R_b , 8.25 mm; d , 1000 μm). As the Length of the package increases, the amplification is also increased (Fig. 8). Initially, when the length of the package is at 10 mm, it gives 16 times amplification. Further, as the package lengths are increased to 15 and 20 mm, the amplification is found to be around 34, 50 times, respectively. However, this increase is found to be linear and rapid until the package length reaches about 20 mm in length, beyond which the amplification factor rises less rapidly. Irrespective of this, it is observed that the highest amplification is 62 times, when the length is chosen as 30 mm. Due to the limitations in the simulation, lengths beyond 30 mm cannot be simulated.

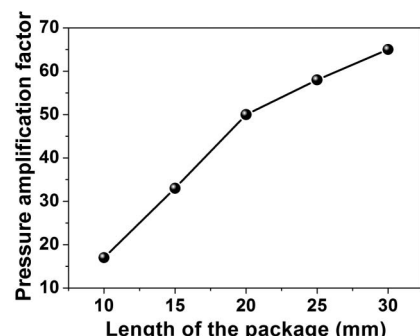


Fig. 8. Plot of pressure amplification factor along the fiber with varying package length.

E. Packaging Material

After finding all the above-mentioned optimized parameters (d , R_b , L , and R) for the highest strain amplification, now it is the packaging material that is considered for the further improvement in strain amplification. Two different packaging materials such as polyimide and RTV3145 have been considered to discover the effect of material properties on stress amplification. The mechanical properties of the chosen materials are listed in Table 2.

At first, pressure of 10^4 Pa is applied to the side-hole package comprised of polyimide as the packaging material. The resultant pressure amplification is measured as 62×10^4 Pa. When the same amount of pressure is applied on the side-hole package comprised of RTV3145, where all other parameters (d , R_b , L , and R) remain unchanged, yielded to the pressure amplification of 110×10^4 Pa. Because the properties such as the Poisson's ratio and density of those materials are similar, this increase in the pressure amplification is solely accredited to their Young's modulus. This is due to the fact that material with a lower Young's modulus is more susceptible to structural deformation, thereby transferring the pressure impact more effectively to the fiber. This result concludes that material with lower Young's modulus promotes higher amplification.

Stress along the cross section of the fiber in an optimized side-hole package is shown in Fig. 9. This plot shows that the stress distribution in the fiber becomes asymmetrical due to external pressure. Side-hole package converts the uniform, symmetrical pressure distribution into an amplified asymmetrical stress distribution along with a stress amplification of around 110 times. Table 3 give the values of optimized parameters of the side-hole package.

These optimized values are given as the input to the electromagnetic module for executing modal analysis. The frequency domain interface of the electromagnetic module is used for modal analysis at a given frequency, v_o . The electromagnetic wave traversing in the fiber core is given by

$$E = E_x(x, y), \quad E_y(x, y), \quad E_z(x, y)e^{i(\omega t - \beta z)}, \quad (7)$$

where E_x , E_y , and E_z are the amplitude of the electric field, along the three axes; ω is the angular frequency; and β is the propagation constant. The effective mode index, $n_{\text{eff}} = \beta/k_o$, is obtained from the Eigenvalues. For the propagation of light,

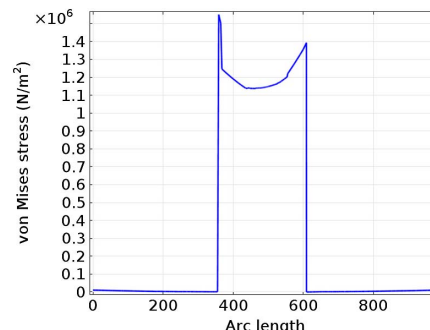
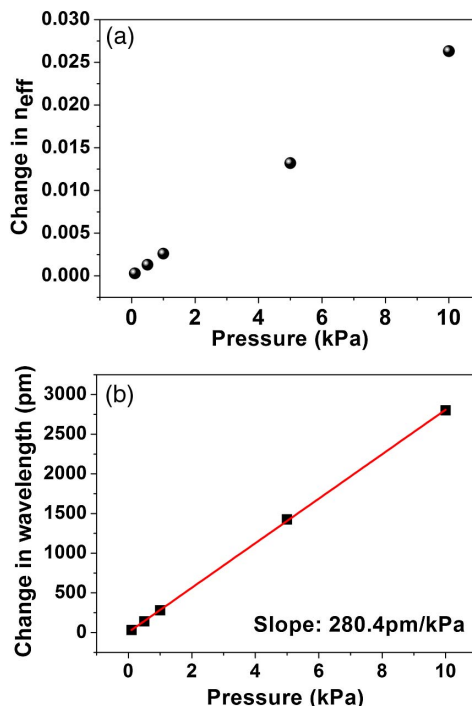


Fig. 9. 1D line graph of Von Mises stress versus distance along a fiber cross section (μm) for a side-hole package of 17.5 mm radius and 3 mm length with side-hole radius of 8.25 mm and package material RTV3145.

Table 3. Optimized Values of Side-Hole Package

Parameters	Value
Radius of the package	17.5 (mm)
Length of the package	30 (mm)
Package material	RTV3145
Hole radius	8.25 (mm)
Distance between the holes	1000 (μm)

**Fig. 10.** (a) Plot of Δn_{eff} with pressure and (b) change in Bragg wavelength with pressure. Red line indicates linear fit of the plot.

at wavelength 1550 nm along the fiber core whose refractive index (n_0) is 1.456, the effective refractive index (n_{eff}) of fundamental mode (LP_{01}) is found to be 1.4548. And the values of n_x , n_y , and n_z , acquired from Eq. (5), are fed into the refractive index tensor in the electromagnetic module. The effective mode index change of the fundamental mode induced by stress, which arises due to the photo-elastic effect of the fiber material, is shown in Fig. 10(a). As a result of stress amplification, due to the side-hole packaging with optimized parameters, it is perceived from the plot that the effective variation in n_{eff} is observed even at 0.1 kPa. It is also observed that the variation in n_{eff} is found to be linear under external pressure.

Taking into consideration the principal strain along the fiber core and n_{eff} change due to applied pressure, the shift in Bragg wavelength is calculated for the FBG sensor using Eq. (6). Figure 10(b) shows the change in Bragg wavelength with respect to the applied external pressure using COMSOL. From the slope of the obtained graph, the response of the side-hole packaged fiber for the pressure sensor is calculated as 280 pm/kPa. This study validates that the sensitivity of fiber could be enhanced from 3 pm/MPa, for a bare FBG sensor, to $\sim 280,000$ pm/MPa, for side-hole packaged FBG sensor,

which is nearly 10^5 times enhancement. These results will be further validated through experiments in a future study.

4. CONCLUSIONS

A comprehensive study of the pressure response of an FBG sensor in a side-hole package has been carried out by the finite element method using COMSOL Multiphysics software. A grating has been introduced at the core of the single-mode fiber with a Bragg wavelength at 1548 nm. Various parameters of the side-hole package, which are affecting the pressure amplification in the fiber, have been optimized using Von Mises stress distribution plots. Simulations demonstrate that an optimized radius and length of the package along with maximum hole radius with a minimum distance of separation between them support maximum pressure amplification in the sensor. Along with this, the choice of the packaging material, with the lowest Young's modulus, promotes the highest-pressure sensitivity. Thus, an optimized side-hole packaged FBG sensor shows a pressure response of nearly 10^5 times as compared with the bare FBG sensor. Such an enhanced pressure response of the FBG sensor is being reported for the first time, which will open the possibilities of detecting acoustic pressure in the range of a few Pascal with FBG sensors.

Funding. DST-INSPIRE Faculty Scheme (DST/INSPIRE/04/2017/000894); Naval Research Board (NRB).

Acknowledgment. The first author thanks the DST-INSPIRE Faculty Scheme for the financial support. The authors would like to thank NRB for the financial assistance to carry out the project. The authors also thank the Supercomputer Education and Research Centre (SERC), IISc, Bangalore, for the technical support for implementing the simulation work.

^{*}These authors contributed equally to this work.

REFERENCES

- G. A. Cranch, P. J. Nash, and C. K. Kirkendall, "Large-scale remotely interrogated arrays of fiber-optic interferometric sensors for underwater acoustic applications," *IEEE Sens. J.* **3**, 19–30 (2003).
- P. J. Nash, G. A. Cranch, and D. J. Hill, "Large-scale multiplexed fiber optic arrays for geophysical applications in environmental and industrial sensing," *Proc. SPIE* **4202**, 55–65 (2000).
- M. Moccia, M. Consale, A. Iadicicco, M. Pisco, A. Cutolo, V. Galdi, and A. Cusano, "Resonant hydrophones based on coated Fiber Bragg Gratings," *J. Lightwave Technol.* **30**, 2472–2481 (2012).
- N. Takahashi, K. Yoshimura, S. Takahashi, and K. Imamura, "Development of an optical fiber hydrophone with fiber Bragg grating," *Ultrasonics* **38**, 581–585 (2000).
- E. Chmielewska, W. Urbańczyk, and W. J. Bock, "Measurement of pressure and temperature sensitivities of a Bragg grating imprinted in a highly birefringent side-hole fiber," *Appl. Opt.* **42**, 6284–6291 (2003).
- S. Campopiano, A. Cutolo, A. Cusano, M. Giordano, G. Parente, G. Lanza, and A. Laudati, "Underwater acoustic sensors based on fiber Bragg gratings," *Sensors* **9**, 4446–4454 (2009).
- S. Huang, X. Jin, J. Zhang, Y. Chen, Y. Wang, Z. Zhou, and J. Ni, "An optical fiber hydrophone using equivalent phase shift fiber Bragg grating for underwater acoustic measurement," *Photon. Sens.* **1**, 289–294 (2011).
- A. Rosenthal, D. Razansky, and V. Ntziachristos, "High-sensitivity compact ultrasonic detector based on a pi-phase-shifted fiber Bragg grating," *Opt. Lett.* **36**, 1833–1835 (2011).

9. L.-Y. Shao, S.-T. Lau, X. Dong, A. P. Zhang, H. L. W. Chan, H. Y. Tam, and S. He, "High-frequency ultrasonic hydrophone based on a cladding-etched DBR fiber laser," *IEEE Photon. Technol. Lett.* **20**, 548–550 (2008).
10. Y. Liu, W. Zhang, T. Xu, J. He, F. Zhang, and F. Li, "Fiber laser sensing system and its applications," *Photon. Sens.* **1**, 43–53 (2011).
11. D. Pawar, C. N. Rao, R. K. Choubey, and S. N. Kale, "Mach-Zehnder interferometric photonic crystal fiber for low acoustic frequency detections," *Appl. Phys. Lett.* **108**, 041912 (2016).
12. H. M. Xie, P. Dabkiewicz, and R. Ulrich, "Side-hole fiber for fiber-optic pressure sensing," *Opt. Lett.* **11**, 333–335 (1986).
13. J. R. Clowes, S. Syngellakis, and M. N. Zervas, "Pressure sensitivity of side-hole optical fiber sensors," *IEEE Photon. Technol. Lett.* **10**, 857–859 (1998).
14. Y. Xin, X. Dong, J. Yuan, Y. Li, S. Jin, and S. Zhang, "Sensing characteristics of side-hole fiber-based long-period grating," *Adv. Mater. Sci. Eng.* **2013**, 850293 (2013).
15. S. H. Lee, B. H. Kim, and W.-T. Han, "Effect of filler metals on the temperature sensitivity of side-hole fiber," *Opt. Express* **17**, 9712–9717 (2009).
16. M. S. Alam and M. A. Islam, "Birefringence properties of side-hole optical fibers," in *International Conference on Communication Technology* (2006).
17. S. Qiufeng and L. Binghua, "Simulation and analysis on hydrostatic pressure sensor using fiber Bragg grating," in *International Conference on Measuring Technology and Mechatronics Automation* (2010).
18. C.-F. Sun, Z.-H. Li, S.-M. Jiao, X.-G. Xu, X.-M. Wang, C.-H. Wang, G.-F. Jin, and S.-X. Wang, "Research on pressure and temperature sensitivities of FBG embedded in novel side-hole package," *Proc. SPIE* **8192**, 81924K (2011).
19. Z. Li, H. Zhu, Z. Tang, and Y. Hu, "Research on fiber Bragg grating side-hole package technology," *Acta Opt. Sinica* **27**, 993–998 (2007).
20. S. Udoth, J. Njuguma, and R. Prabhu, "Modelling and simulation of fiber Bragg grating characterization for oil and gas sensing applications," *Int. J. Simul. Syst. Technol.* **15**, 213–218 (2014).
21. Y. Wang, X. Qiao, H. Yang, D. Su, L. Li, and T. Guo, "Sensitivity-improved strain sensor over a large range of temperatures using an etched and regenerated fiber Bragg grating," *Sensors* **14**, 18575–18582 (2014).
22. C. Wu, J. Li, X. Feng, B.-O. Guan, and H.-Y. Tam, "Side-hole photonic crystal fiber with ultrahigh polarimetric pressure sensitivity," *J. Lightwave Technol.* **29**, 943–948 (2011).
23. C. Wu, B.-O. Guan, Z. Wang, and X. Feng, "Characterization of pressure response of Bragg gratings in grapefruit microstructured fibers," *J. Lightwave Technol.* **28**, 1392–1397 (2010).